Supporting formation for

Fully Quantized Electron Transfer Observed in a Single Redox Molecule at a Metal Interface

Antoine Roy-Gobeil,[1] Yoichi Miyahara,[1], Kirk H. Bevan[2], Peter Grutter,[1]

[1]Department of Physics, McGill University,

3600 rue University, Montréal, Québec H3A 2T8, Canada

[2]Division of Materials Engineering, Faculty of Engineering, McGill University,

Montréal, Québec H3A 0C5, Canada

S1. THEORY

S1.1. Quantized Electron Transfer Model with Vibrons

S1.1.1. Single-Vibrational Mode Model

For a single-vibrational mode, the nuclear Hamiltonian for the reduced and oxidized molecular configurations, respectively, can be written as [1, 2]

$$\hat{H}_{\rm mol} = E_{\rm red} + -\frac{\hbar^2}{2\mathcal{M}}\frac{\partial^2}{\partial x^2} + \frac{1}{2}\mathcal{M}\omega^2 x^2 \tag{S1}$$

$$\hat{H}^{+}_{\rm mol} = E_{\rm ox} + -\frac{\hbar^2}{2\mathcal{M}}\frac{\partial^2}{\partial x^2} + \frac{1}{2}\mathcal{M}\omega^2 (x - \sqrt{2}\zeta l)^2 \tag{S2}$$

where x represents its coordinate, $\mathcal{M}$ its mass, ω its frequency, ζ its dimensionless electron-vibronic coupling parameter [2], and the characteristic length is given by $l = (\hbar/\mathcal{M}\omega)^{1/2}$. Here we assume that the mass and frequency of a vibrational mode do not change upon oxidation/reduction. Moreover, to remain consistent with our ferrocene (Fc) molecule under examination, a positive charge superscript ($^+$) is appended to distinguish the oxidized Fc^+ Hamiltonian from the reduced Fc Hamiltonian. For the single mode Hamiltonian, the nuclear wavefunctions and energies are given by

$$\hat{H}_{\rm mol}\chi_m = \big(E_{\rm red} + (1/2 + m)\hbar\omega\big)\chi_m \tag{S3}$$

$$\hat{H}^{+}_{\rm mol}\chi^{+}_n = \big(E_{\rm ox} + (1/2 + n)\hbar\omega\big)\chi^{+}_n. \tag{S4}$$

here we use vibronic indices m and n for the reduced and oxidized configurations, respectively. The equilibrium occupation probability of each vibronic eigenstate is given by

$$P_m \approx e^{-m\hbar\omega_j/k_{\rm B}T}(1 - e^{-\hbar\omega_j/k_{\rm B}T}) \tag{S5}$$

$$P^{+}_n \approx e^{-n\hbar\omega_j/k_{\rm B}T}(1 - e^{-\hbar\omega_j/k_{\rm B}T}) \tag{S6}$$

and is arrived at by defining a partition function for the mode [3]. Experimentally, we have determined that the lowest lying mode observed is of the energy $\hbar\omega_1 = 11.6 k_B T = 4.6$ meV at $T = 4.7$ K. This corresponds to an equilibrated occupation of probability of nearly 1 for the zero-point vibronic eigenstates. That is, $P_0 \approx 1$ and $P^{+}_0 \approx 1$, similarly $P_{m\geq 1} \approx 0$ and $P^{+}_{n\geq 1} \approx 0$, at $T = 4.7$ K.

Now, the electron transfer rate between two configurations within the total energy picture is expressed as [1, 4]

$$k_{i\to f} \approx \frac{2\pi}{\hbar}|M|^2|\langle\chi_i|\chi_f\rangle|^2\,\delta(E_i - E_f) \tag{S7}$$

where E_i and E_f are the initial (i) and final (f) state *total energies*, $|M|^2$ is the electronic coupling, and $\hbar$ is Planck's constant. Here we use a slightly different index notation from the main text, to avoid confusion with vibrational mode energies in this more expansive discussion. Note that in the voltage-biased systems, *total energy* is in fact the Helmholtz free energy which includes the work done by voltage sources [4].

An equivalent representation can be written within the single-particle energy picture in the form [5]

$$k_{i\to f} \approx \frac{2\pi}{\hbar}|M|^2\,|\langle\chi_i|\chi_f\rangle|^2\,\delta(\varepsilon_i - \varepsilon_f) \tag{S8}$$

where ε_i and ε_f are the initial and final state *single-particle* energies [5]. A single-particle energy represents the cost of adding/removing an electron; so if two single-particle energies are the same, then the total energy is also conserved in an electron transfer event between them [5]. The primary difference between the two pictures, is how the electronic coupling $|M|^2$ is computed. Eq. (S8) uses single-particle electron wavefunctions, while Eq. (S7) utilizes many-body electronic wavefunctions (which are needed to arrive at total energy electronic eigenstates). In our analysis, the electronic coupling is approximated as a constant ($|M|^2$), so the choice of representation is a matter of convenience. Here we utilize the single-particle picture to describe the electron transfer rate to/from a single-particle state in the gold substrate from/to a single-particle state in Fc/Fc^+. Since, there exists a range of single-particle energies (ε) inside the gold substrate (S) in the form of a density-of-states (D_S), our electron transfer rate to single-particle energy ε_m on the oxidized Fc^+ molecule can be written as [5, 6]

$$k_{S\to m} = \frac{2\pi}{\hbar}|M|^2\left|\left\langle\chi_0^+\middle|\chi_m\right\rangle\right|^2\int D_S(\varepsilon)f(\varepsilon)\delta(\varepsilon-\varepsilon_m)d\varepsilon. \tag{S9}$$

Note, we are assuming that the molecule is thermally equilibrated prior to electron transfer in the χ_0^+ zero-point oxidized state ($n=0$) at $T = 4.7$ K, as discussed above, and is transitioning to the reduced state vibronic configuration χ_m. For this transition, the oxidized configuration single-particle energies are given by $\varepsilon = \varepsilon_{\text{mol}} + m\hbar\omega$, with $\varepsilon_{\text{mol}} = E_{\text{red}} - E_{\text{ox}}$. In the absence

of electron-vibronic coupling, $\varepsilon_{\mathrm{mol}} = E_{\mathrm{red}} - E_{\mathrm{ox}}$ is the single-particle energy for electron addition/removal (e.g., highest occupied molecular orbital energy). The substrate states are occupied according the Fermi-Dirac distribution

$$f(\varepsilon) = \frac{1}{1 + e^{(\varepsilon - \varepsilon_{\mathrm{F}})/k_{\mathrm{B}}T}} \tag{S10}$$

with respect to the Fermi energy, ε_{F} (see Fig. 3b in the main manuscript). Eq. (S9) is an extension of Eq. (S8), whereby a transition between two states is converted to an integrated summation over all possible originating states in the gold substrate weighted by their occupation probability [1, 6]. Likewise, the electron transfer rate from single-particle energy state ε_n on a Fc group in the reduced configuration, to empty states in the substrate is given by

$$k_{n\to S} = \frac{2\pi}{\hbar}|M|^2 \left|\langle\chi_0|\chi_n^+\rangle\right|^2 \int D_{\mathrm{S}}(\varepsilon)[1 - f(\varepsilon)]\delta(\varepsilon - \varepsilon_n)d\varepsilon \tag{S11}$$

where the single-particle energies that the electron may depart from on the molecule are given by $\varepsilon_n = \varepsilon_{\mathrm{mol}} - n\hbar\omega$. To arrive at the forward and backwards electron transfer rates (k_f and k_b) we sum over all possible transitions

$$k_f = \sum_m k_{S\to m} = \frac{2\pi}{\hbar}|M|^2 D_{\mathrm{S}} \int f(\varepsilon) \sum_m \Big[\left|\langle\chi_0^+|\chi_m\rangle\right|^2 \delta(\varepsilon - \varepsilon_{\mathrm{mol}} - m\hbar\omega)\Big] d\varepsilon \tag{S12}$$

$$k_b = \sum_n k_{n\to S} = \frac{2\pi}{\hbar}|M|^2 D_{\mathrm{S}} \int [1 - f(\varepsilon)] \sum_n \Big[\left|\langle\chi_0|\chi_n^+\rangle\right|^2 \delta(\varepsilon - \varepsilon_{\mathrm{mol}} + n\hbar\omega)\Big] d\varepsilon. \tag{S13}$$

To simplify the calculation process we have treated D_{S} as a constant, which is typical for a metal substrate such as gold [1, 2, 5, 6]. The summations that we have brought into each integral represent the quantum version of the oxidized (D_{ox}) and reduced (D_{red}) density-of-states in the low temperature limit [1, 5–7]

$$\left[D_{\mathrm{ox}}\right]_{k_{\mathrm{B}}T \ll \hbar\omega} = \sum_m \Big[\left|\langle\chi_0^+|\chi_m\rangle\right|^2 \delta(\varepsilon - \varepsilon_{\mathrm{mol}} - m\hbar\omega)\Big] \tag{S14}$$

$$[D_{\mathrm{red}}]_{k_{\mathrm{B}}T \ll \hbar\omega} = \sum_n \Big[\left|\langle\chi_0|\chi_n^+\rangle\right|^2 \delta(\varepsilon - \varepsilon_{\mathrm{mol}} + n\hbar\omega)\Big]. \tag{S15}$$

for a single vibrational mode in the spirit of Gerischer as shown in Fig. 3b in the main manuscript [1, 6]. These distributions are normalized since $\sum_m \left|\langle\chi_0^+|\chi_m\rangle\right|^2 = 1$ and $\sum_n \left|\langle\chi_0|\chi_n^+\rangle\right|^2 = 1$. At room temperature ($k_{\mathrm{B}}T \approx 25$ meV) for a single vibrational mode in the energy range $\hbar\omega \ll k_{\mathrm{B}}T$, the quantum distribution recovers the semi-classical Gerischer

distribution [1, 5–8]

$$\left[D_{\mathrm{ox}}\right]_{k_{\mathrm{B}}T\gg\hbar\omega} = \frac{1}{\sqrt{4\pi\lambda k_{\mathrm{B}}T}}\exp\!\left(\frac{-(\varepsilon-\varepsilon_{\mathrm{mol}}-\lambda)^2}{4\lambda k_{\mathrm{B}}T}\right) \tag{S16}$$

$$\left[D_{\mathrm{red}}\right]_{k_{\mathrm{B}}T\gg\hbar\omega} = \frac{1}{\sqrt{4\pi\lambda k_{\mathrm{B}}T}}\exp\!\left(\frac{-(\varepsilon-\varepsilon_{\mathrm{mol}}+\lambda)^2}{4\lambda k_{\mathrm{B}}T}\right). \tag{S17}$$

This is accomplished after incorporating the high temperature equilibrium occupation probabilities (P_m and P_n^+) and accounting for transitions from vibronic states above the zero-point energy [9].

S1.1.2. Relation to the More Realistic Multi-Mode Vibronic System

In this section we discuss why the formerly presented simplified single-mode model is suitable for the system under study. In general a molecule such as Fc will possess multiple vibrational modes with frequencies ω_j. Under this broader scenario, the nuclear Hamiltonian for the reduced and oxidized molecular configurations, respectively, can be written as [1]

$$\hat{\mathcal{H}}_{\mathrm{mol}} = E_{\mathrm{red}} + \sum_{j=1}^{N}\Big(-\frac{\hbar^2}{2\mathcal{M}_j}\frac{\partial^2}{\partial x_j^2} + \frac{1}{2}\mathcal{M}_j\omega_j^2 x_j^2\Big) \tag{S18}$$

$$\hat{\mathcal{H}}_{\mathrm{mol}}^{+} = E_{\mathrm{ox}} + \sum_{j=1}^{N}\Big(-\frac{\hbar^2}{2\mathcal{M}_j}\frac{\partial^2}{\partial x_j^2} + \frac{1}{2}\mathcal{M}_j\omega_j^2 (x_j-\sqrt{2}\zeta_j l_j)^2\Big) \tag{S19}$$

where x_j represents the normal coordinate of a given vibrational mode, $\mathcal{M}_j$ its mass, ω_j its frequency, ζ_j its dimensionless electron-vibronic coupling parameter [2], and the characteristic length of each mode is given by $l_j = (\hbar/\mathcal{M}_j\omega_j)^{1/2}$. Again, we assume that the mass and frequency of a mode do not change upon oxidation/reduction. The eigenstates and eigenenergies of each vibrational mode are given by

$$\hat{\mathcal{H}}_{\mathrm{mol}}\tilde{\chi}_{j,m} = \big(E_{\mathrm{red}} + (1/2+m)\hbar\omega_j\big)\tilde{\chi}_{j,m} \tag{S20}$$

$$\hat{\mathcal{H}}_{\mathrm{mol}}^{+}\tilde{\chi}_{j,n}^{+} = \big(E_{\mathrm{ox}} + (1/2+n)\hbar\omega_j\big)\tilde{\chi}_{j,n}^{+}. \tag{S21}$$

Just as was done with the single-vibrational mode, here we use vibronic index m for the reduced state and vibronic index n for the oxidized state. The heterogeneous reorganization energy of each vibrational mode is given by $\lambda_j = \zeta_j^2\hbar\omega_j$ [2], such that the total heterogeneous reorganization energy of the molecule is [10]

$$\lambda_{\mathrm{tot}} = \sum_{j=1}^{N}\lambda_j. \tag{S22}$$

It is important to note that λ_{tot} is the quantity typically associated with room temperature electron transfer experiments, however in our measurements only the lowest lying vibrational mode ω_1 (and therefore reorganization energy λ_1) drives nuclear coupling dependence in the electron transfer events explored. Hence, our application of a single-mode model to interpret the experimental data.

There are two reasons for this. Firstly, the small bias applied between the molecule and substrate is only sufficient to excite the lowest lying vibrational mode ($\hbar\omega_1 = 4.6$ meV). The next highest vibrational mode for isolated Fc has been measured in earlier work to be $\hbar\omega_2 \approx 22.3$ meV [11]. Secondly, the temperature of the system (4.7 K) drives the zero-point energy occupation for each vibrational mode very close to 1 (as discussed previously for a single-vibrational mode). In this low temperature limit, the overall equilibrium nuclear wavefunction for the system in the reduced and ground states can be expressed as [1, 12]

$$\chi_0 = \frac{1}{\sqrt{N!}}\mathcal{P}\big[\prod_{j=1}^{N}\tilde{\chi}_{j,0}(x_j)\big] \tag{S23}$$

$$\chi_0^+ = \frac{1}{\sqrt{N!}}\mathcal{P}\big[\prod_{j=1}^{N}\tilde{\chi}_{j,0}^+(x_j)\big]. \tag{S24}$$

across the set of vibronic coordinates $\{x_j\}$. The operator $\mathcal{P}$ produces N-factorial permutations of the nuclear eigenstate coordinate assignments to provide a symmetric boson wavefunction. Now, since the low bias applied between the molecule and substrate is only able to excite the lowest lying vibrational mode ($\hbar\omega_1$), our transitions are to excited states of the form

$$\chi_m = \frac{1}{\sqrt{N!}}\mathcal{P}\big[\tilde{\chi}_{1,m}(x_1)\prod_{j=2}^{N}\tilde{\chi}_{j,0}(x_j)\big] \tag{S25}$$

$$\chi_n^+ = \frac{1}{\sqrt{N!}}\mathcal{P}\big[\tilde{\chi}_{1,n}^+(x_1)\prod_{j=2}^{N}\tilde{\chi}_{j,0}^+(x_j)\big]. \tag{S26}$$

The corresponding Franck-Condon coupling factors for transition for the reduced configuration to the oxidized configuration are then given by

$$|\left\langle\chi_0\middle|\chi_n^+\right\rangle|^2 = |\left\langle\tilde{\chi}_{1,0}\middle|\tilde{\chi}_{1,n}^+\right\rangle|^2\prod_{j=2}^{N}|\left\langle\tilde{\chi}_{j,0}\middle|\tilde{\chi}_{j,0}^+\right\rangle|^2 + c.c \approx |\left\langle\tilde{\chi}_{1,0}\middle|\tilde{\chi}_{1,n}^+\right\rangle|^2\prod_{j=2}^{N}|\left\langle\tilde{\chi}_{j,0}\middle|\tilde{\chi}_{j,0}^+\right\rangle|^2 \tag{S27}$$

and that from the oxidized configuration to the reduced configuration are likewise

$$|\left\langle \chi_0^+ \middle| \chi_m \right\rangle|^2 = |\left\langle \tilde{\chi}_{1,0}^+ \middle| \tilde{\chi}_{1,m} \right\rangle|^2 \prod_{j=2}^{N} |\left\langle \tilde{\chi}_{j,0}^+ \middle| \tilde{\chi}_{j,0} \right\rangle|^2 + c.c. \approx |\left\langle \tilde{\chi}_{1,0}^+ \middle| \tilde{\chi}_{1,m} \right\rangle|^2 \prod_{j=2}^{N} |\left\langle \tilde{\chi}_{j,0}^+ \middle| \tilde{\chi}_{j,0} \right\rangle|^2. \tag{S28}$$

Again, here we assume that the molecule reaches thermal equilibrium prior to each electron transfer event. We have also assumed that the cross coupling terms between vibrational modes are negligible ($c.c. \approx 0$). Importantly, under this approximation, coupling contributions for all high energy vibrational modes ($j \geq 2$) resolve out to constant factor ($\prod_{j=2}^{N} |\left\langle \tilde{\chi}_{j,0}^+ \middle| \tilde{\chi}_{j,0} \right\rangle|^2 = \prod_{j=2}^{N} |\left\langle \tilde{\chi}_{j,0} \middle| \tilde{\chi}_{j,0}^+ \right\rangle|^2$) for the low energy excitations considered. Thus, it the lowest lying mode reorganization and vibronic energies (λ_1 and $\hbar\omega_1$) which are primarily of concern in the electron transfer events we have explored.

S1.2. Electron Transfer Rates Expressions for Biased System

Within our AFM system, an electron transfer event is facilitated by shifting the gold substrate Fermi energy (ε_{F}) with respect to the molecule level by an amount $-e\alpha(z(t))V_{\mathrm{B}}$ (see Fig. 1 in the main manuscript) [13], which controls energy detuning that describes the offset between $\varepsilon_{\mathrm{mol}}$ and ε_{F} in the form $\Delta\varepsilon(t) = \varepsilon_{\mathrm{F}} - e\alpha(z(t))V_{\mathrm{B}} - \varepsilon_{\mathrm{mol}}$. The detuning varies in time due to the sinusoidal oscillation of the AFM tip. When $\Delta\varepsilon = 0$, the molecular eigenstate is brought into resonance (or "in tune") with substrate Fermi-level by the applied bias. To account for these specific measurement details, we have found it helpful to write electron transfer rates for our AFM system in terms of t and V_{B} with the form

$$k_f\big(t, V_{\mathrm{B}}\big) = \frac{2\pi}{\hbar}|M|^2 D_{\mathrm{S}} \int f(\varepsilon - e\alpha(z(t))V_{\mathrm{B}}) \sum_m \Big[\left|\left\langle \chi_0^+ \middle| \chi_m \right\rangle\right|^2 \delta(\varepsilon - \varepsilon_{\mathrm{mol}} - m\hbar\omega)\Big] d\varepsilon \tag{S29}$$

$$k_b\big(t, V_{\mathrm{B}}\big) = \frac{2\pi}{\hbar}|M|^2 D_{\mathrm{S}} \int [1 - f(\varepsilon - e\alpha(z(t))V_{\mathrm{B}})] \sum_n \Big[\left|\left\langle \chi_0 \middle| \chi_n^+ \right\rangle\right|^2 \delta(\varepsilon - \varepsilon_{\mathrm{mol}} + n\hbar\omega)\Big] d\varepsilon. \tag{S30}$$

Examples of k_f and k_b are plotted as a function of time in Fig. S1(c) and (d), respectively.

S1.3. Atomic Force Microscopy Model

In the experiments, the AFM tip is used both as a movable gate and a sensitive charge sensor by forming a single-electron box with the molecule and the back-electrode[14]. For a

small cantilever oscillation compared to the tip-molecule separation, the capacitance of the tip varies linearly with z and the interaction Hamiltonian can be linearized:

$$H_{\rm int} = A\, n\, z \tag{S31}$$

where z is the position of the cantilever and $A \equiv -eV_{\rm B}\dfrac{d\alpha}{dz} = \dfrac{d\Delta\varepsilon}{dz}$ is the molecule-AFM coupling strength [15]. The cantilever is described as a driven, damped harmonic oscillator with a resonance frequency, f_0, spring constant, c and quality factor, Q. Since during the experiment, the trajectory of the oscillator remains harmonic ($z(t) = \bar{z} + d\,\cos(2\pi f_0 t)$) and the frequency shift due to electron tunneling is small ($\Delta f \ll f_0$), the description of the coupled electromechanical system is dramatically simplified by focusing on the simpler dynamics of system averages, an approach justified by comparison with full simulations [16] This results in time-dependent forward and backward tunneling rates $k_f(\Delta\varepsilon(t))$ and $k_b(\Delta\varepsilon(t))$ to respectively add and remove an electron from the molecule. In turn, this perturbation modulates the average charge occupation, $p(t)$, through the rate equation

$$\frac{\partial p}{\partial t} = -k_b(\Delta\varepsilon(t))\, p + k_f(\Delta\varepsilon(t))\,(1-p) \tag{S32}$$

which is measured as an electrostatic force acting on the tip, $F(t) = A\,p(t)$. The in-phase component of that force, with respect to the motion of the tip, will result in a frequency shift [16]

$$\Delta f = -\frac{f_0^2}{cd}\int_0^{1/f_0} F(t)\cos(2\pi f_0 t)\, dt. \tag{S33}$$

This is illustrated in Fig. S1 where the time trajectories discussed above are evaluated in order to obtain the frequency shift response Δf. First, we have the cantilever tip trajectory $z(t)$ (Fig. S1a). Second, the energy detuning as a function of time $\Delta\varepsilon(z(t))$ (Fig. S1b) created by the cantilever tip oscillation. Third, we compute the tunneling rates $k_f(\Delta\varepsilon(t))$ and $k_b(\Delta\varepsilon(t))$ as a function of time (Fig. S1c). Fourth, using those rates, we compute the charge response of the molecule, $p(t)$, which satisfies Eq. S32 (Fig. S1d). Finally, the cantilever resonance frequency will shift proportionally to the in-phase component of the back-action force $F(t) = A\,p(t)$ to its motion according to Eq. S33.

S2. OVERVIEW IMAGES OF THE SAMPLE

Figure S2 shows the frequency shift and dissipation images of the sample with larger scan area. Multiple charge rings are clearly seen in the dissipation image which indicate the

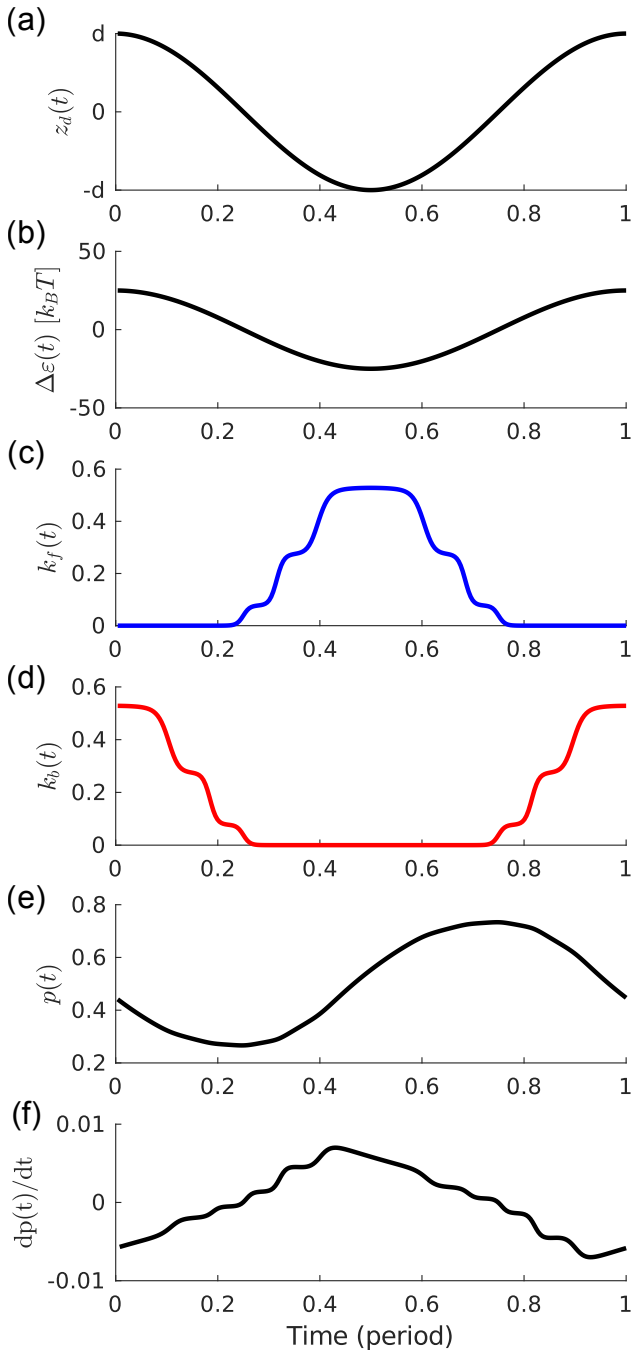

FIG. S1. Time trajectories of the mean values of interest over one tip oscillation period. a) Position of the cantilever. b) Energy detuning in time, $\Delta\varepsilon$, controlled by the mean tip-sample distance or bias V_{B} with a fixed harmonic modulation $Ad = 60k_{\mathrm{B}}T$. c,d) Associated tunneling rates in and out assuming parameters $\zeta = 1.67$, $\hbar\omega = 25k_{\mathrm{B}}T$ and $\Gamma = \pi f_0$. e) Average charge on the molecule, expressed as a probability of occupation $p(t)$, obtained by solving the simplified rate equation Eq. S32. f) Time derivative of probability $p(t)$ clearly reveals the effect of discrete jumps in tunneling rates due to the opening of additional vibronic transitions.

variability of the surrounding environment of Fc groups in the sample. It is important to note that the rings are much more difficult to be seen in the frequency shift image because the contribution of the topography to the image contrast often overwhelms the contrast due to the charging (rings).

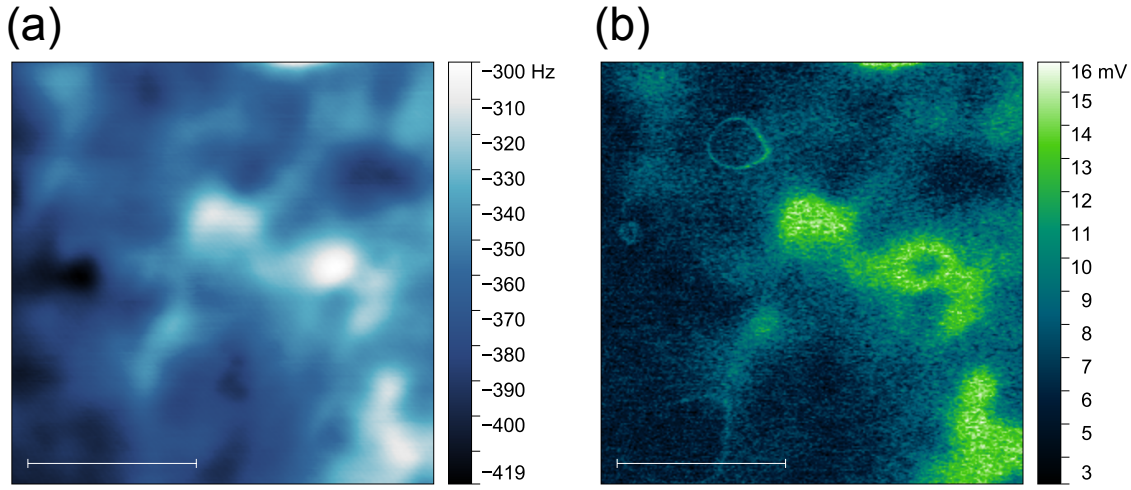

FIG. S2. Constant-height frequency shift and dissipation images with larger scan area taken at $V_B = 5$ V. Scale bar is 400 nm.

S3. AFM ENERGY CALIBRATION

S3.0.1. Lever-arm α

In a linear regime where $k_f(\Delta\varepsilon(t))$ and $k_b(\Delta\varepsilon(t))$ linearly depends on the energy detuning $\Delta\varepsilon(t)$, the above problem is analytically solvable and the frequency shift is given by:

$$\Delta f = -\frac{f_0 A^2}{2c} \frac{(k_f'(k_f + k_b) - k_f(k_f + k_b)')}{(k_f + k_b)^2 + \omega^2} \tag{S34}$$

where $'$ denotes derivative with respect to energy evaluated at the mean value of $\Delta\varepsilon$ [17, 18].

In Figure S3, we estimate the value of α from a fit to the peak shape measured at the lowest oscillation amplitude obtaining a value of $\bar{\alpha} = 0.035$.

S3.0.2. Coupling strength A

The coupling strength, A, is computed from the evolution of the charging peak's width as the oscillation amplitude, d, is increased. Because energy is conserved upon tunneling,

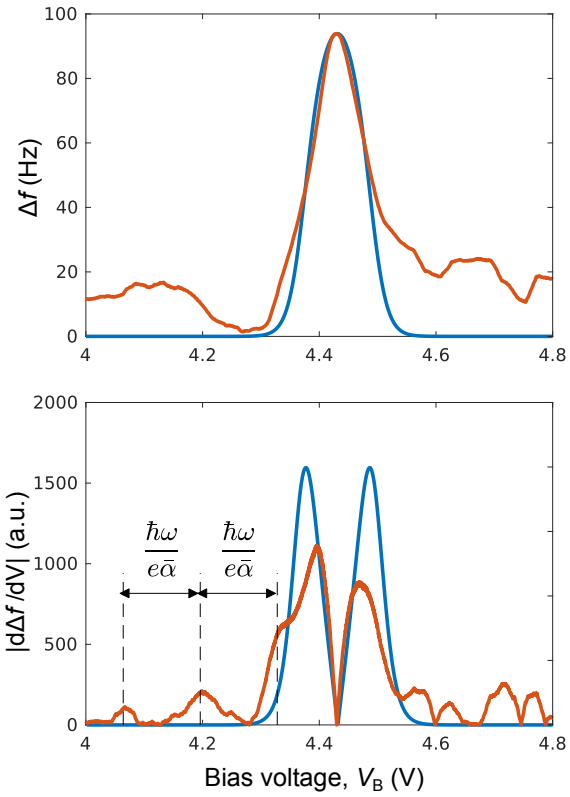

FIG. S3. AFM frequency shift response (top) and its derivative with respect to the bias voltage V_{B} (bottom) acquired at oscillation amplitude $d = 0.1$ nm (red line) compared with theory (blue line) using the model parameters $\zeta = 1.67$ and $\hbar\omega = 11.6\ k_{\mathrm{B}}T = 4.6$ meV. The lever-arm and its first derivative were calibrated to be $\alpha = 0.035$ and $A = -eV_{\mathrm{B}}\, d\alpha/dz = 36$ meV/nm.

signal will only appear in the range of V_{B} given by $V_{\mathrm{B}} = [V_{\mathrm{B}}^0 - \dfrac{A}{e\bar{\alpha}}d, V_{\mathrm{B}}^0 + \dfrac{A}{e\bar{\alpha}}d]$ where V_{B}^0 is the charging peak's center position (which corresponds to $\Delta\varepsilon = 0$ as explained in the main text). Note that the quantity, Ad, is approximately equal to $\delta\Delta\varepsilon$ which is the maximum change in the energy detuning, $\Delta\varepsilon(z(t))$, caused by $z(t)$. The bias range for which this condition is met will enlarge as the oscillation amplitude, d, increases. We estimate the width of this bias range for each measured spectrum by identifying the smallest and the largest values of V_{B} at which the signal is observed (marked as circles in Fig. S4a). Using those values, we compute the peaks' half width and in Fig. S4b), we compare the values at different oscillation amplitudes, d. The two quantities are linearly related by a slope $\dfrac{A}{e\bar{\alpha}}$. By performing a least-square fit regression of the form

$$\frac{A}{e\bar{\alpha}}d + \text{const.} = \text{half width at base} \tag{S35}$$

we extract the coupling strength, A, to be $1.0\,\bar{\alpha}$ eV/nm ($A = 35$ meV/nm for $\bar{\alpha} = 0.035$ obtained in the previous section). This calibration procedure has been tested for accuracy by analyzing theoretical peak shapes of known coupling strength. The A extracted by the procedure above underestimated the theoretical values by roughly 5%.

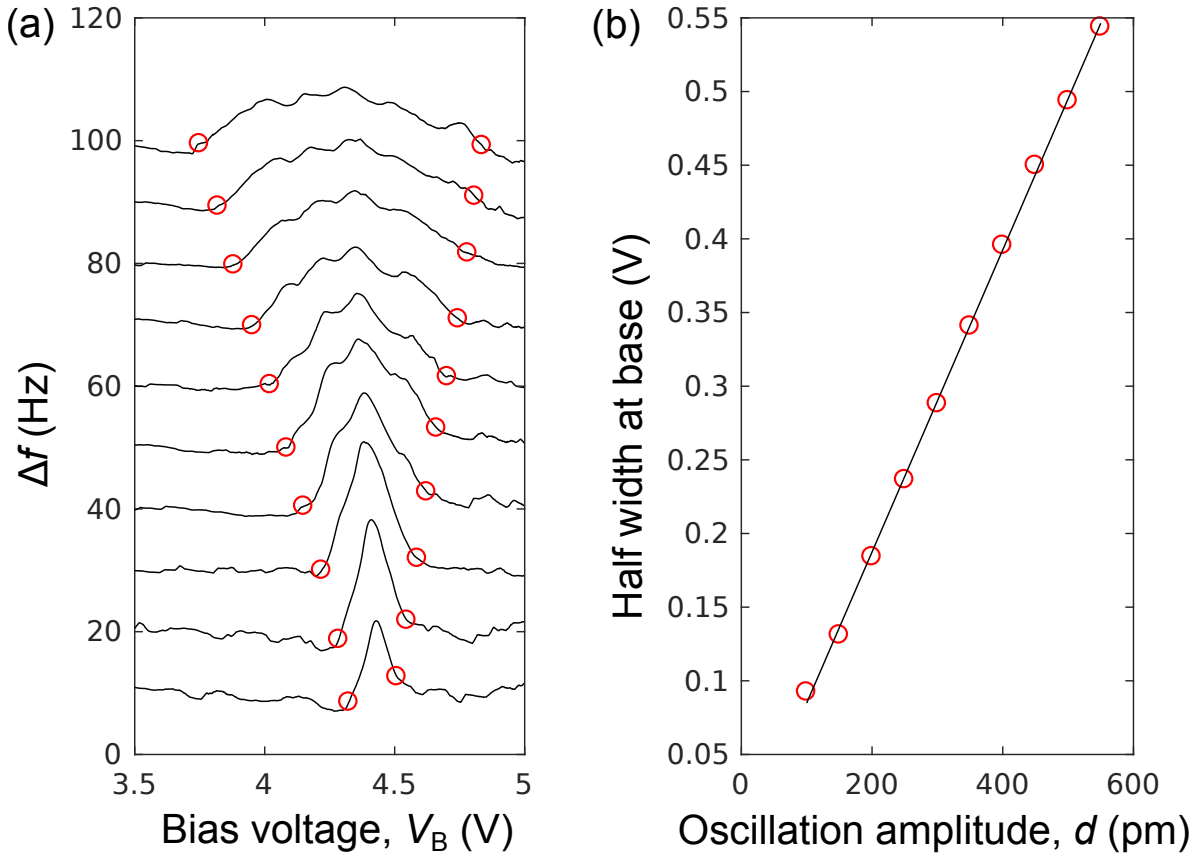

FIG. S4. a) Frequency shift (Δf) spectra, with increasing AFM oscillation amplitude, above a Fc group. Red circles indicate biases at which tunneling becomes allowable and hence charging start to develop. b) Half width of the charging peak at base versus oscillation amplitude d. The black line is a linear regression yielding a slope $\frac{A}{\bar{\alpha}}$ of 1.0 mV/pm.

S4. MOVIE S1 AND S2

Schematic representation of the electron transfer process between the metallic electrode and Fc group at a small tip oscillation amplitude of 0.10 nm in which $\Delta\varepsilon \ll \hbar\omega$ (S1) and at a large tip oscillation amplitude of 0.35 nm in which $\Delta\varepsilon > \hbar\omega$ (S2). V_B is being swept throughout each movie as time evolves.

(a) Schematic of the AFM experimental setup. An oscillating AFM cantilever tip is capacitively coupled to the molecule in vacuum. A dc bias voltage, V_{B}, that is applied between the tip and substrate causes a voltage drop, $\alpha(z)V_{\mathrm{B}}$, across the tunnel barrier between the metallic substrate and the molecule of interest. For a small tip oscillation amplitude, d, compared to the mean tip-sample distance, $\bar{z}$, the voltage drop is modulated in time as $\alpha(t) \approx \alpha(\bar{z}) + \frac{d\alpha}{dz} d\cos(2\pi f_0 t)$ (inset).

(b) Potential profile along the line passing through the AFM tip and Fc group under a contant V_{B}. As the tip oscillates vertically, the potential at the molecule oscillates accordingly.

(c) Schematic representation of the free energy of the Fc (red) and Fc^+ (blue) redox state under a DC bias, V_{B}. The holizontal axis is the nuclear coordinate. The potential energy of the molecule is approximated as a parabola. The equillibrium coordinates of the reduced (red) and oxidized (blue) states are shifted by $\sqrt{2}\zeta$ where ζ is an electron-nuclear coupling strength. The nuclear wavefunctions are drawn at each corresponding energy in each parabola.

(d) Schematic energy single-particle energy diagram of the metal-Fc system. The electrons in the metallic electrode follow Fermi-Dirac distribution. The nuclear coupling weighted electron transition probabilities are represented by blue lines for Fc^+ to Fc state transition and by red lines for Fc to Fc^+ state transition.

(e) Associated forward (k_f) and backward (k_b) electron transfer rates as a function of the energy detuning, $\Delta\varepsilon$. Nuclear vibronic transitions are separated by quantized vibronic energy, $\hbar\omega$ whose origin is the molecular single-particle energy $\varepsilon_{\mathrm{mol}}$.

(f) Time trajectories of the electron transfer rate as well as the associated average charge occupation, $p(t)$, solution to Eq. S32.

(g) The experimental (orange curve) and theoretical (black curve) frequency shift response of the AFM calculated from Eq. S33.

S4.1. Description of Movie S1 (small oscillation amplitude case)

Sequence 1 (from 00:00 to 00:25): $\Delta\varepsilon$ remains below 0, leading to $k_b > 0$ but $k_f = 0$ throughout the whole oscillation periods. As a result, $p(t)$ remains zero. No Δf response results.

Sequence 2 (from 0:25 to 00:42): $\Delta\varepsilon$ can alternate between $\Delta\varepsilon > 0$ and $\Delta\varepsilon < 0$ in response to the tip oscillation, enabling tunneling-in (reduction) and tunneling-out (oxidation) in one oscillation period. As a result, $p(t)$ oscillates. Δf signal increases as $\bar{\Delta}\varepsilon$ reaches 0.
Sequence 3 (from 0:43 to the end): $\Delta\varepsilon$ remains above 0, leading to $k_b = 0$ but $k_f > 0$ throughout the whole oscillation periods. As a result, $p(t)$ remains one. No Δf response results.

S4.2. Description of Movie S2 (large oscillation amplitude case)

Sequence 1 (from 00:00 to 00:04): $\Delta\varepsilon$ remains below 0, leading to $k_b > 0$ but $k_f = 0$ throughout the whole oscillation periods. As a result, $p(t)$ remains zero. No Δf response results.
Sequence 2 (from 0:05 to 00:42): $\Delta\varepsilon$ can alternate between $\Delta\varepsilon > 0$ and $\Delta\varepsilon < 0$ in response to the tip oscillation, enabling tunneling-in (reduction) and tunneling-out (oxidation) in one oscillation period. As a result, $p(t)$ oscillates. Δf signal increases as $\overline{\Delta\varepsilon}$ reaches 0 (0:33). Each time $\Delta\varepsilon$ reaches the next peak of the transition probability (shown as lines in (d)), k_b (or/and k_f) changes stepwise manner, resulting in increase in the amplitude of $p(t)$.
Sequence 3 (from 0:43 to the end): $\Delta\varepsilon$ remains above 0, leading to $k_b = 0$ but $k_f > 0$ throughout the whole oscillation periods. As a result, $p(t)$ remains one. No Δf response results.

[1] W. Schmickler, *Interfacial Electrochemistry*, 1st ed. (Oxford University Press, 1996).

[2] J. Koch, F. von Oppen, and A. V. Andreev, Phys. Rev. B **74**, 205438 (2006).

[3] L. D. Landau and E. M. Lifshitz, *Statistical Physics*, 3rd ed. (Butterworth-Heinemann, 2013).

[4] C. Wasshuber, *Computational Single-Electronics*, Computational Microelectronics (Springer Vienna, Vienna, 2001).

[5] K. H. Bevan, J. Chem. Phys. **146**, 134106 (2017).

[6] K. H. Bevan, M. S. Hossain, A. Iqbal, and Z. Wang, J. Phys. Chem. C **120**, 179 (2016).

[7] A. Nitzan, *Chemical dynamics in condensed phases: Relaxation, Transfer, and Reactions in Condensed Molecular Systems* (Oxford University Press, 2006).

[8] M. Bixon and J. Jortner, in *Advances in Chemical Physics* (John Wiley & Sons, Inc., 1999) pp. 35–202.

[9] C. E. Patrick and F. Giustino, Journal of Physics: Condensed Matter **26**, 365503 (2014).

[10] Note, the heterogeneous reorganization energy is half of the homogenous reorganization energy commonly utilized in Marcus-Hush theory [1, 5].

[11] E. Kemner, I. M. de Schepper, G. J. Kearley, and U. A. Jayasooriya, J. Chem. Phys. **112**, 10926 (2000).

[12] D. J. Griffiths, *Introduction to Quantum Mechanics*, 2nd ed. (Pearson, 2004).

[13] M. S. Hossain and K. H. Bevan, J. Phys. Chem. C **120**, 188 (2016).

[14] R. Stomp, Y. Miyahara, S. Schaer, Q. Sun, H. Guo, P. Grutter, S. Studenikin, P. Poole, and A. Sachrajda, Phys. Rev. Lett. **94**, 056802 (2005).

[15] Y. Miyahara, A. Roy-Gobeil, and P. Grutter, Nanotechnology **28**, 064001 (2017).

[16] S. D. Bennett, L. Cockins, Y. Miyahara, P. Grütter, and A. A. Clerk, Physical Review Letters **104**, 017203 (2010).

[17] L. Cockins, Y. Miyahara, S. D. Bennett, A. A. Clerk, S. Studenikin, P. Poole, A. Sachrajda, and P. Grutter, Proc. Natl. Acad. Sci. U.S.A. **107**, 9496 (2010).

[18] A. Roy-Gobeil, Y. Miyahara, and P. Grutter, Nano Lett. **15**, 2324 (2015).